

LNF-94/047 (IR)  
22 Settembre 1994

L. Benussi, M. Bertani, S. Bianco, F.L. Fabbri, P. Gianotti, M. Giardoni,  
C. Guaraldo, A. Lanaro, V. Lucherini, A. Mecozzi, L. Passamonti, V. Russo,  
S. Sarwar:

**HIGH PERFORMANCE TRACKING WITH LONG STRAW TUBES  
USING DIMETHYL ETHER**

**PACS.: 29.40.Gx**

# High Performance Tracking with Long Straw Tubes using Dimethyl Ether.

L. Benussi, M. Bertani, S. Bianco, F.L. Fabbri,  
P. Gianotti, M. Giardoni, C. Guaraldo, A. Lanaro, V. Lucherini,  
A. Mecozzi, L. Passamonti, V. Russo, and S. Sarwar.

*Laboratori Nazionali di Frascati,  
Via E. Fermi 40, I-00044 Frascati, Italy*

## Abstract

A cylindrical tracking detector with an inner radius of one meter employing straw tubes is being envisaged for the FINUDA experiment aimed at hyper-nuclear physics at DAΦNE, the Frascati  $\phi$ -factory. A prototype using several 10 mm and 20 mm diameter, two meter long aluminized mylar straws has been assembled and tested with a one GeV/c pion beam. While operating with dimethyl ether gas gain, space resolution, and device systematics have been studied. A simple method of correction for systematics due to straw eccentricity has been developed and, once applied, a space resolution better than 40  $\mu$ m can be reached.

## 1 Introduction

The FINUDA [1],[2] experiment is planned to have an outer tracking device employing about 2500 straw tubes. The straws are divided in one axial and two  $\pm 15^\circ$  stereo super-layers. The axial super layer is the innermost at a radial distance of 111 cm from the beam axis. Each of the three super-layers are subdivided in two layers of 15 mm diameter straws, staggered by approximately one straw radius. The straw length as determined by the required geometrical acceptance is greater than 2 m.

In order to investigate the straw tube performance, a prototype using several two meter long, 10 mm and 20 mm diameter, aluminized mylar straws has been assembled at LNF. Operating with pure dimethyl ether signal characteristics, single's count rate plateau, and gas gain were studied. The prototype was tested with a one GeV/c  $\pi^-$  beam at CERN while studying straw space resolution and device systematics. In this work, the prototype construction details and the results from the above mentioned studies are reported.

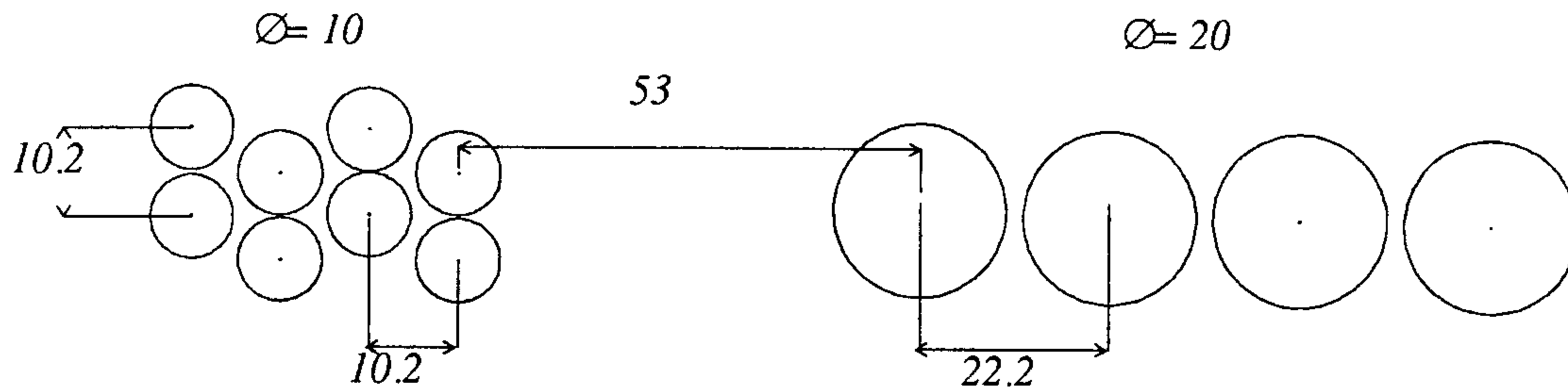


Figure 1: Prototype geometrical details. All dimensions are in millimeters.

## 2 Prototype construction details

The geometrical details of the prototype array are shown in fig.1. It employs eight two meter long straws with an inner diameter of  $10 \pm 0.05 \text{ mm}$  and four  $20 \pm 0.05 \text{ mm}$  diameter straws. The 10 mm straws are arranged in four staggered layers, each containing 2 straws. The layers are staggered by 5.1 mm. The four 20 mm straws are all aligned and placed at  $\sim 5 \text{ cm}$  from the staggered straws.

The used straws [3] are produced by spiral wrapping of a 0.012 mm thick vacuum aluminized mylar strip on a mandrel. The aluminum thickness is 0.1 micron. A coat of polyester-based epoxy is applied on the wrapped strip and a second, 0.012 mm thick, mylar strip is wrapped over it. The overall straw thickness is  $0.03 \pm 0.01 \text{ mm}$ , which represents about  $1 \times 10^{-4}$  radiation lengths. The weight density is  $\sim 1.3 \text{ g/m}$  for 10 mm diameter straws and  $2.6 \text{ g/m}$  for 20 mm diameter straws.

Gold plated tungsten wires [4] with a diameter of 0.03 mm have been used as anode. The wire resistance is measured to be  $85 \Omega/\text{m}$ . The maximum load supported by a wire is 1.8 N.

The anode wire is crimped in gold plated copper pins shown in fig.2. The pin has an inner hole of  $0.10 \pm 0.02 \text{ mm}$  with a 6 mm long crimping zone which has an outer diameter of  $0.70 \pm 0.01 \text{ mm}$ . The 10 mm long conic section of the pin, covered by acetal resin, gives it the mechanical rigidity and positions it at the center of the straw feedthrough.

The feedthrough as shown in fig.3 consists of an aluminum cylinder which, on the straw side, has an external diameter (tapered by 10 % at the beginning) equal to the straw inner diameter with a tolerance of 0.01 mm. The inner surface of the straw is glued on to feedthrough using a silver-based conductive glue. The endplate side of the feedthrough is externally threaded which when tightened with the corresponding nut permits the feedthrough to move along the axis of the endplate hole while pulling the straw to the required tension. The feedthrough contains an inner delrin body which accommodates the wire pin and provides the gas inlet/outlet for the straws.

In the final assembly the prototype straws are supported at the two ends only. In order to minimize the gravitational sag, these are subjected to a pulling force of

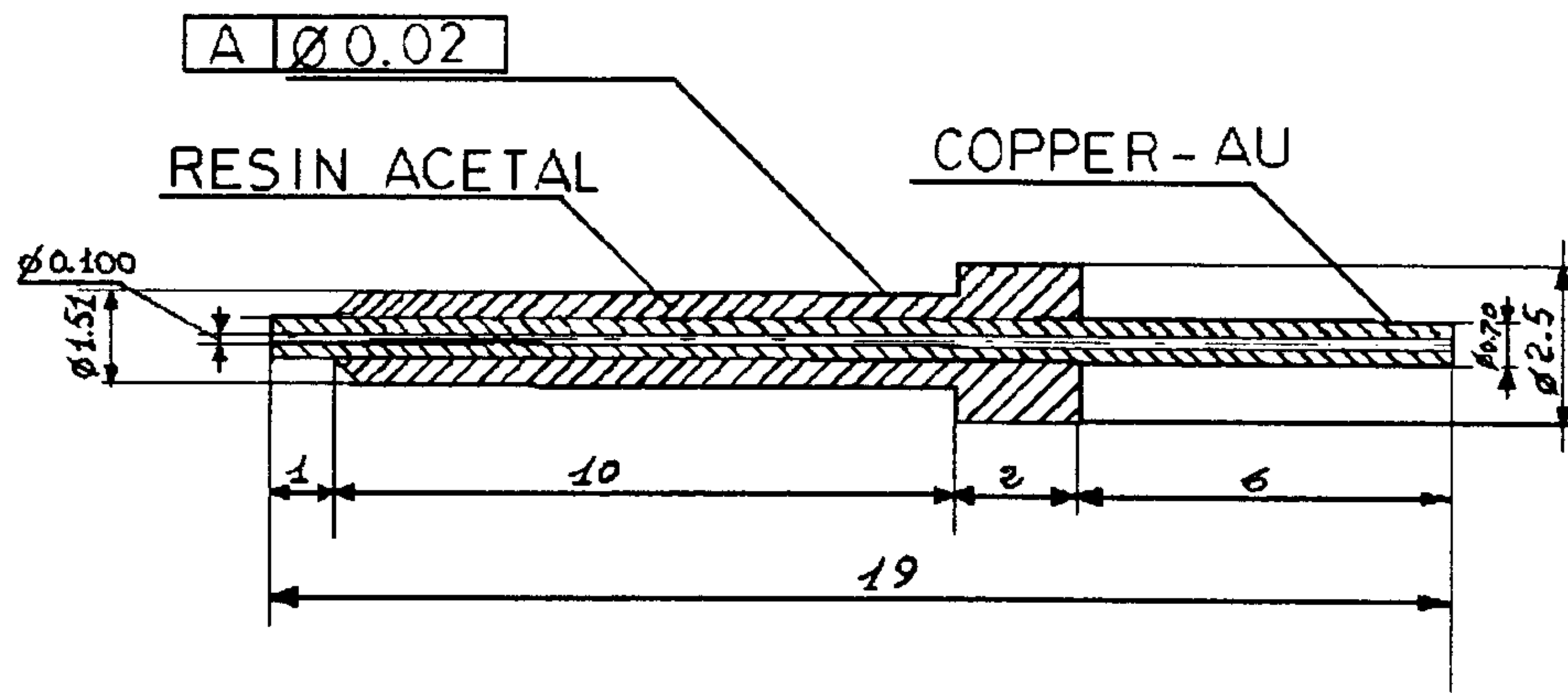


Figure 2: Design features of the pin. All dimensions are in millimeters.

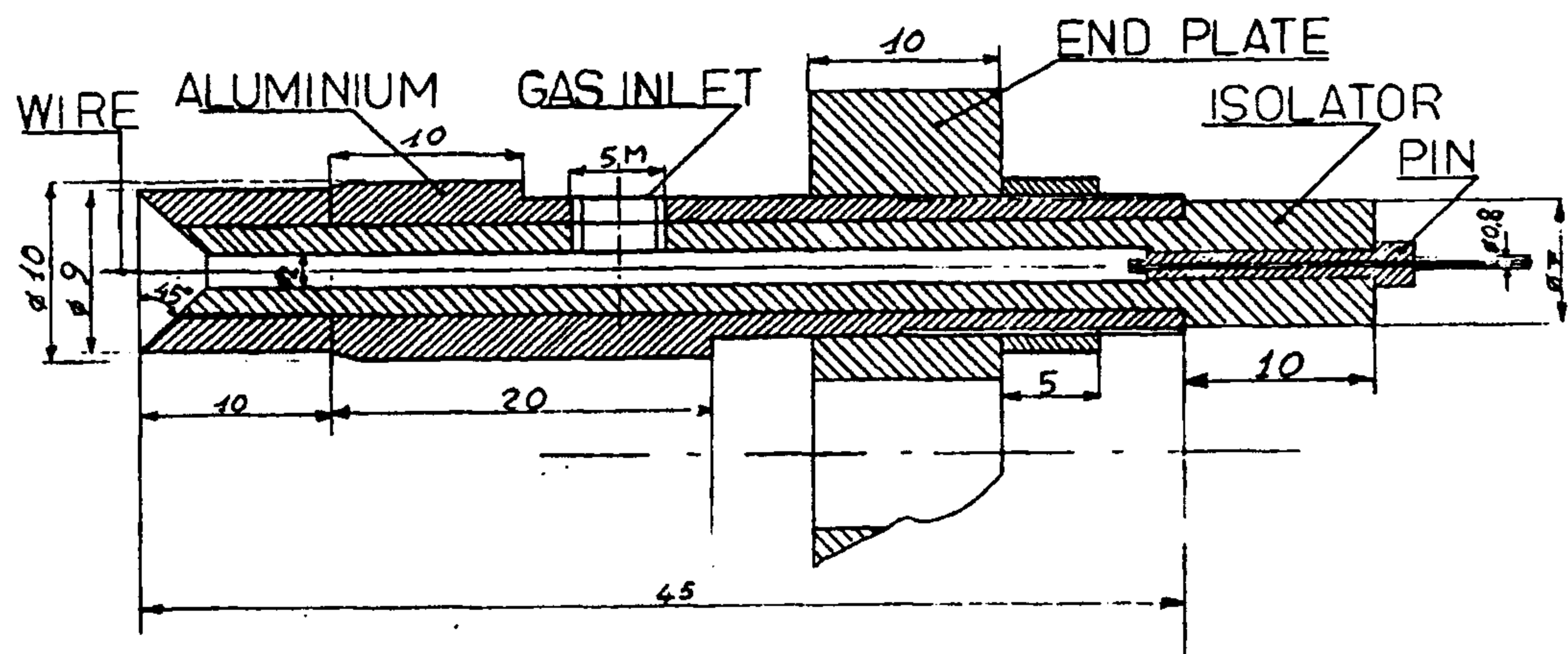


Figure 3: Feedthrough design. All dimensions are in millimeters.

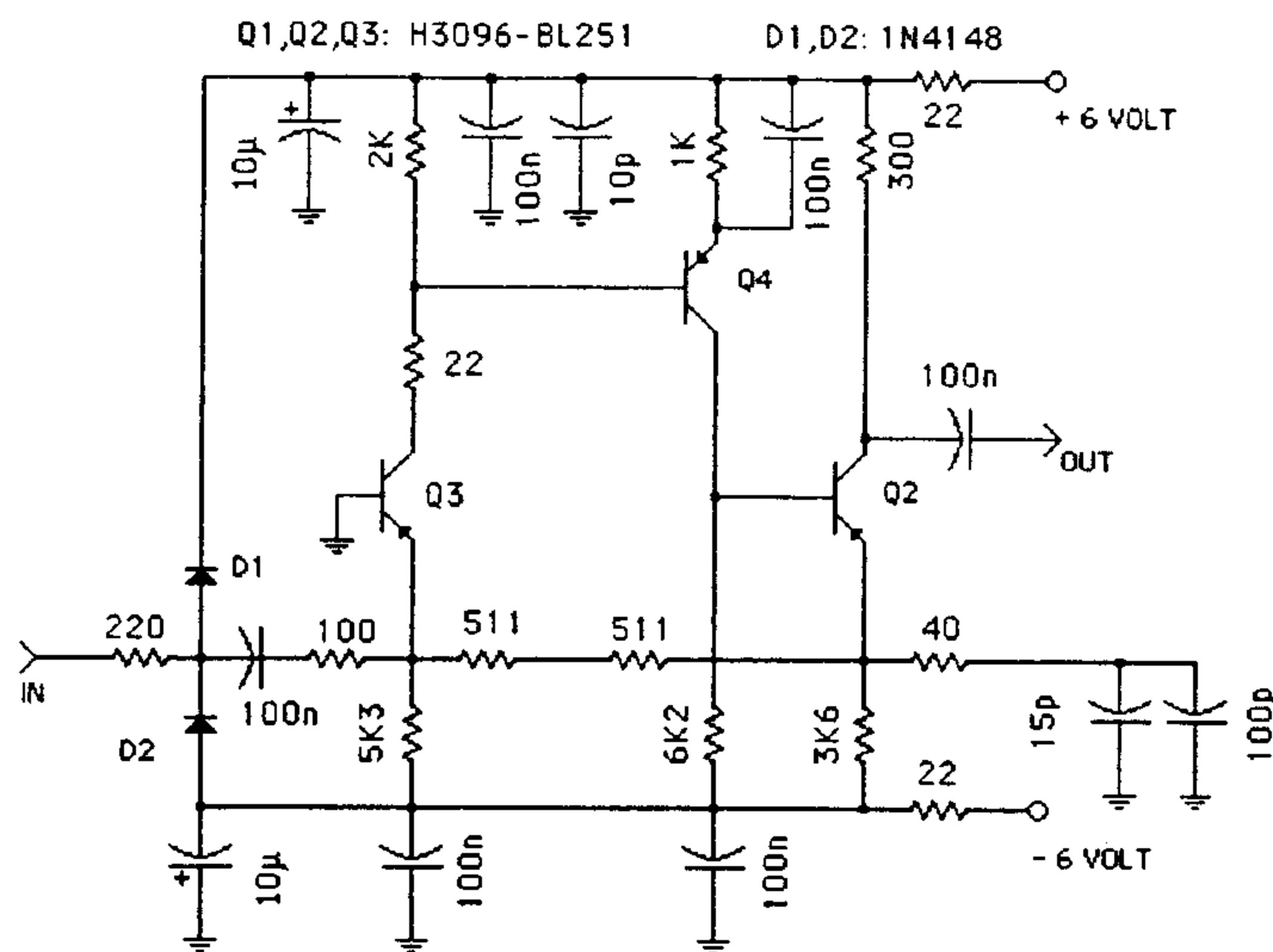


Figure 4: Circuit diagram of the preamplifier.

25  $N$ . As the straws are pulled their length is increased with each  $N$  of the tension giving rise to a relative elongation of  $\sim 0.02\%$ . Straws are therefore cut to be 1  $cm$  shorter than their final length of 2  $m$ .

Table 1: Preamplifier characteristics.

Input impedance	300 $\Omega$
Output impedance	50 $\Omega$
Gain	1-3 $V/mA$
Charge gain	20-60
Dynamic range	2 $V$
Output rise time	2 $ns$
Power supply	$\pm 6 V$
Power consumption	50 $mW$

During the assembly the wire is initially strung through the straw, feedthroughs, and the pins without any mechanical tension. The inner surface of the straw on the two ends is now glued [5] on to feedthroughs. The setting time of the glue is 16 hours at room temperature and once hardened it has a tensile strength of 126  $kg/cm^2$ . When the glue is hardened, feedthroughs are inserted in the endplates and the straw is tensioned to 25  $N$ . After blocking the feedthroughs against the endplates the wire is crimped inside the pin on one of the straw ends tensioned to 1  $N$  and crimped on the opposite end.

The preamplifiers (fig.4) were mounted on printed circuit boards using surface mount devices. The input impedance of the circuit is 300  $\Omega$ . Three different preamplifier gain values (1, 2 and 3  $V/mA$ ) have been employed on the prototype. The circuit operates with  $\pm 6 V$  dissipating 50  $mW$  per channel. The maximum output

pulse height before the saturation sets in is  $2 V$ . The preamplifier characteristics are summarized in Tab.1. In order to provide e.m. shielding the preamplifiers were enclosed in brass boxes and connection to straws were provided by  $\sim 5 cm$  long coaxial cables with the grounded shield.

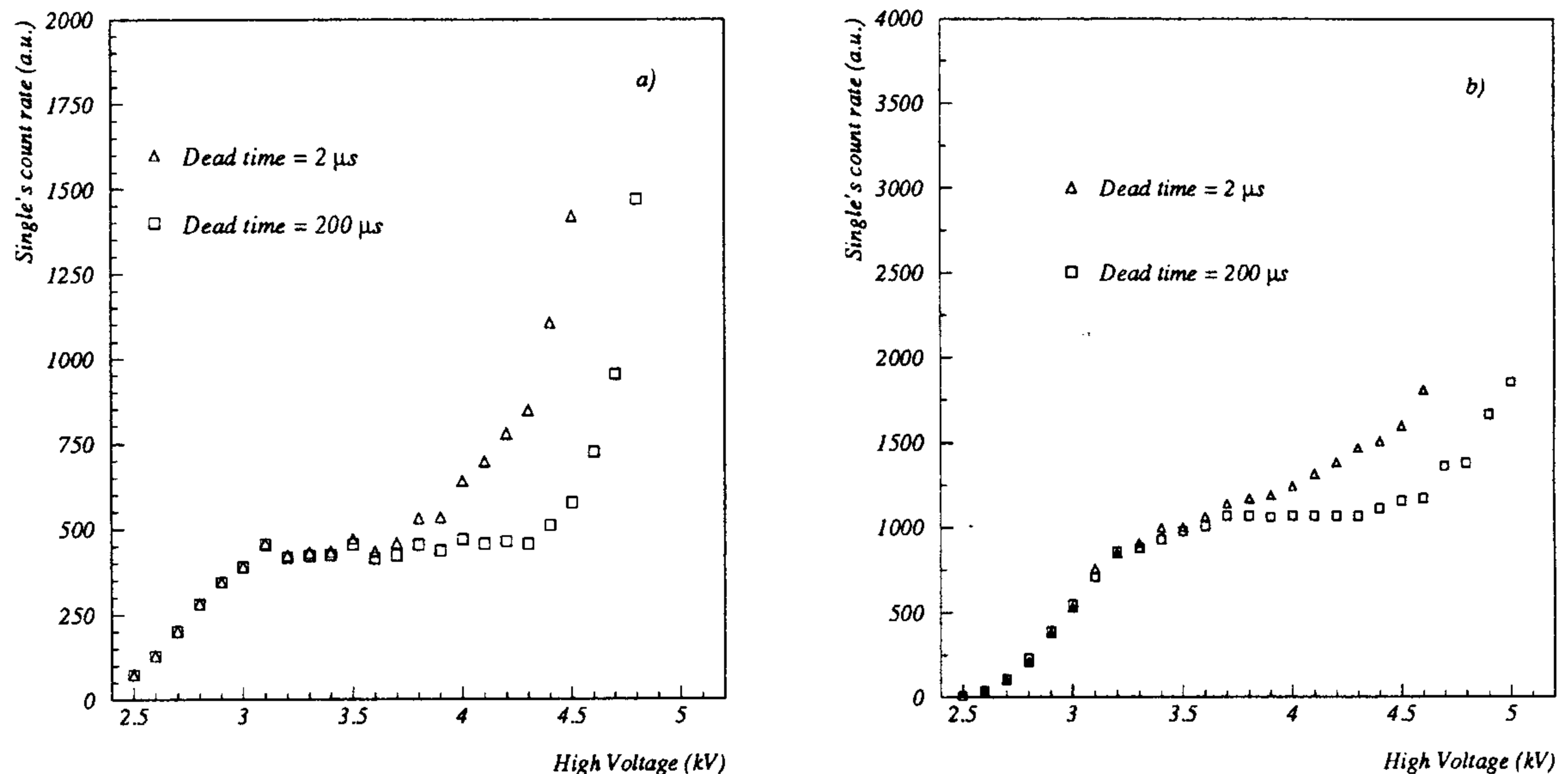


Figure 5: Typical single's count rate plateau curves for a) 10 mm straws, b) 20 mm straws.

### 3 Signal characteristics and gas gain

The gas used with the prototype was 99.8% pure dimethyl ether at an overpressure of  $\sim 20 mbar$ . The high voltage was switched on after five volume changes and a constant flow of 2 straw volumes/day was used during data taking.

All the 10 mm diameter straws reach a single's count rate plateau at about 3 kV of the applied high voltage and typically the plateau is more than 800 V long (fig.5a). The plateau knee for 20 mm straws is found at 3.2 kV. The signals (fig.6) for cosmic rays and ambient radioactivity, observed at the output of the preamplifier with anode at 500 V above the plateau knee show an average of 200 mV of pulse height with a rise time of 3 ns.

Gas gain was measured using pulses originated by single electrons produced by photoemission from cathode surface. By illuminating the straw with a torch light, an electron emission rate of 8 kHz was produced, which was much higher than the single's rate so that the gain measurements were not biased. On the other hand, this rate was low enough to ensure that the probability to integrate more than one pulse in the same ADC gate was negligible. Typical ADC charge distributions for a 10 mm straw at two different voltage settings is shown in fig.7.

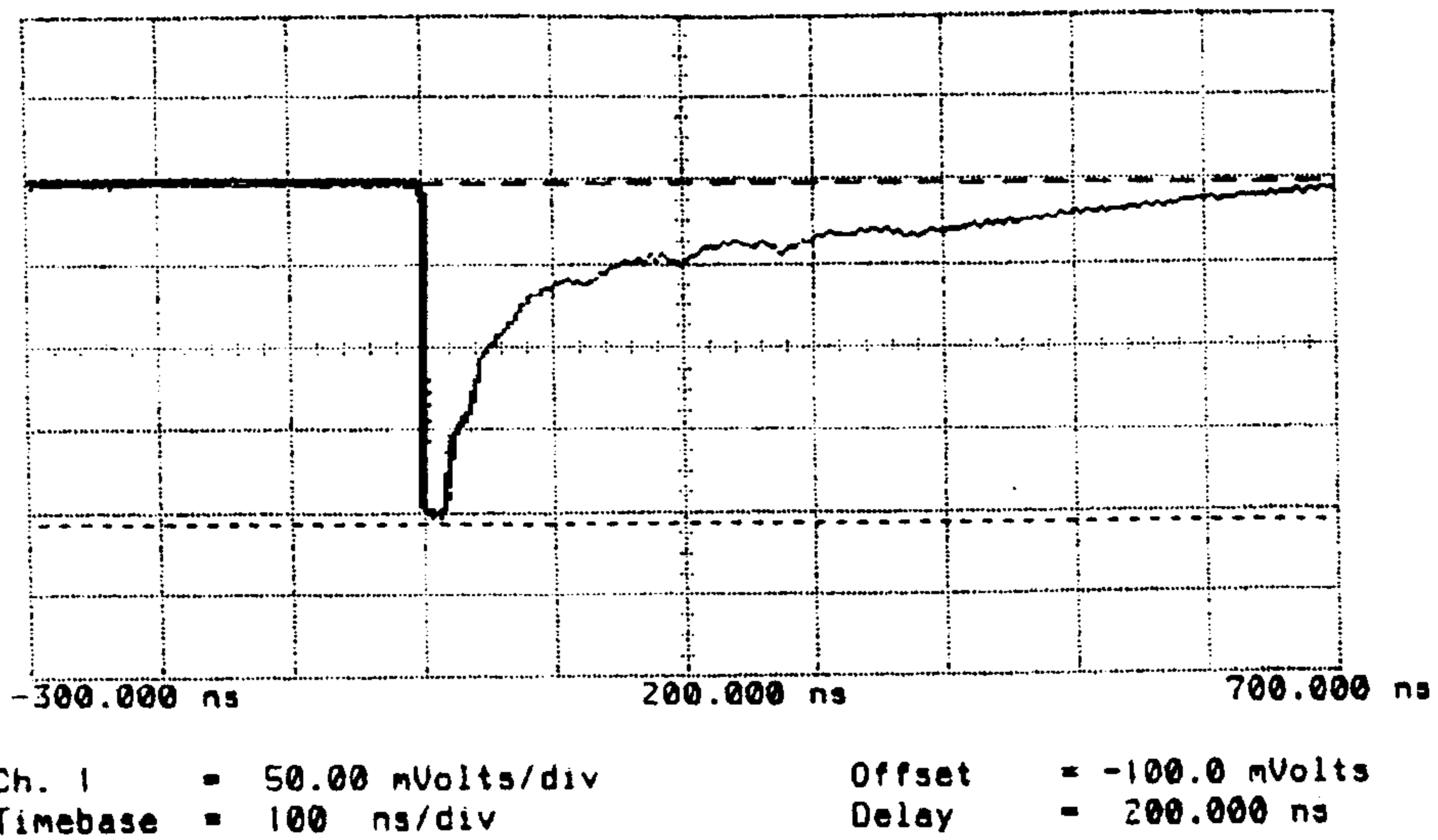


Figure 6: Average signal shape at the output of the preamplifier.

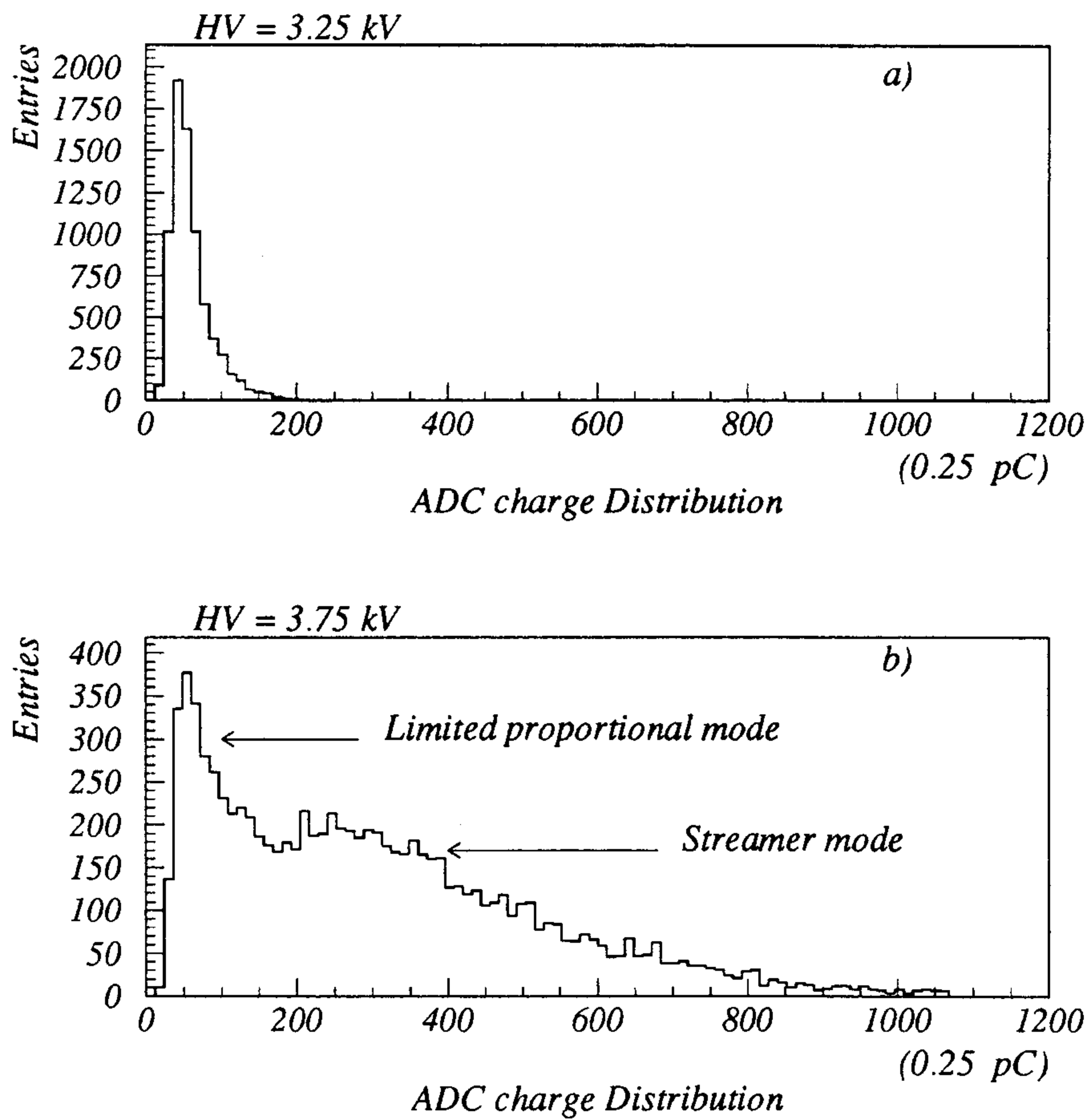


Figure 7: ADC charge distributions for avalanches started by single electrons.

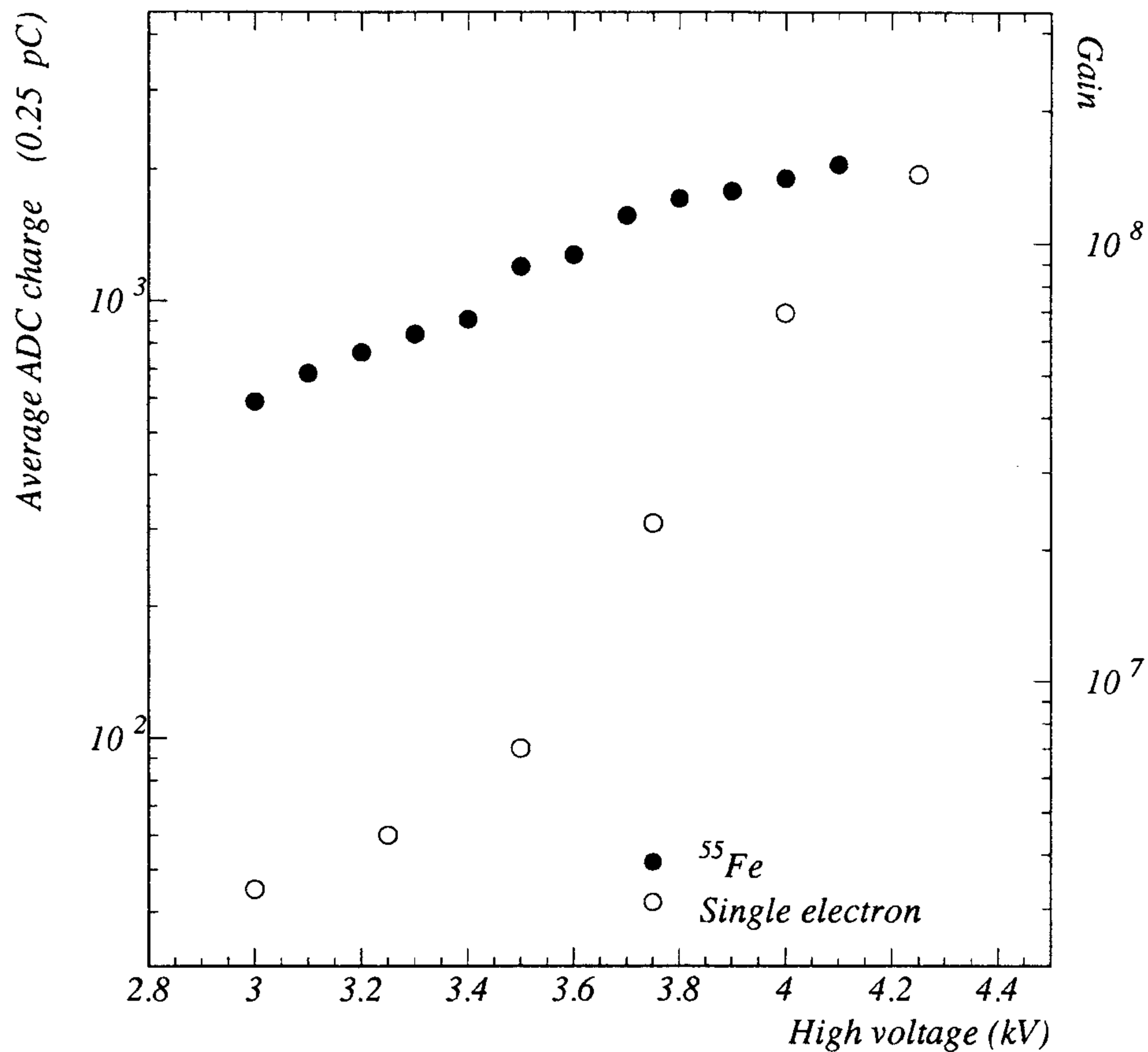


Figure 8: Average ADC charge for single electron and  $^{55}\text{Fe}$  signals. The scale for gas gain to be read with single electron signals is shown on the left.

The gas gain  $G_{gas}$  is obtained from average ADC charge  $\langle ADC \rangle$  by:

$$G_{gas} = \frac{\langle ADC \rangle}{e G_{preamp}} \quad (1)$$

where  $G_{preamp}$  is the charge gain of preamplifier and  $e$  is the electron charge. The gain variations with straw voltage are shown in fig.8.

To investigate the mode of operation we additionally used the signal from  $^{55}\text{Fe}$  source. The  $^{55}\text{Fe}$  source with its characteristic 5.9 keV X-ray emission is expected to produce a tight cluster of  $\sim 200$  electrons. The average value of ADC charge,  $\langle ADC \rangle$ , against applied voltage is shown in fig.8 for  $^{55}\text{Fe}$  source and can be compared with single electron signals. At 3.7 kV the single electron signals show a jump in gas gain, eventually reaching almost the same value of  $^{55}\text{Fe}$  signals, indicating a transition from limited proportional to streamer mode.



## 4 Test with pion beam

The prototype array was tested with a one  $GeV/c$   $\pi^-$  beam at CERN. The test beam setup is shown in fig.9. The 20  $mm$  diameter straws were facing the beam incoming direction followed by 10  $mm$  diameter straws. The prototype was mounted on a support moveable both in horizontal and vertical direction, which permitted us to scan the straw along the wire axis. The straws were operated with pure dimethyl ether (99.8%) at an overpressure of 20  $mbar$ . The anode voltage was set to 3200  $V$  for the 10  $mm$  straws and to 3500  $V$  for the 20  $mm$  straws.

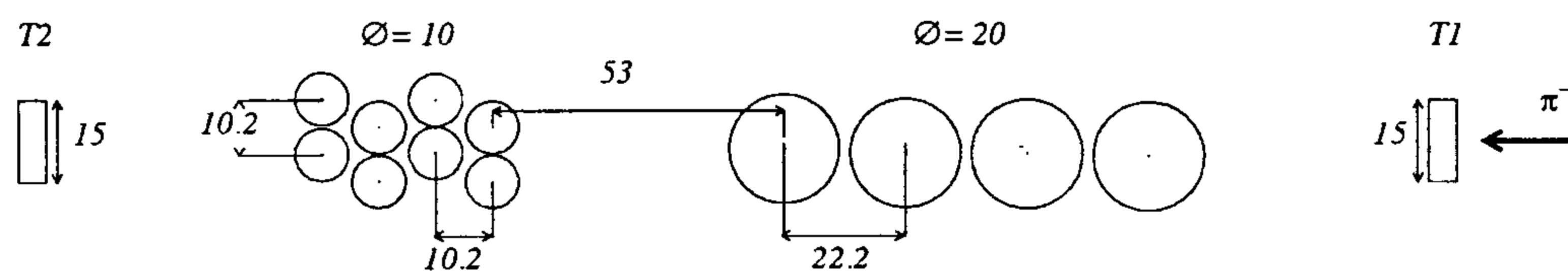


Figure 9: CERN test beam setup. All dimensions are in millimeters.

A pair of scintillators was used to define a  $\sim 15 \times 15$   $mm^2$  beam spot. Coincidence of these two gave the start signal to TDCs.

The preamplifiers were mounted immediately after the straw ends. The amplified straw signals were brought to discriminators, operated with a threshold of  $-30$   $mV$ , by 6  $m$  of RG-58 cables. CAEN model N96 discriminators were used for the 10  $mm$  diameter straws whereas CAEN N224 discriminators were employed for the 20  $mm$  straws. The discriminator output was brought to stop input of TDCs by 40  $m$  long RG-58 cables. Drift times were read for both 10 and 20  $mm$  straws using 12 bit TDCs (CAEN C414) operated in common start mode. In order to have the maximum drift time within the TDC range, with best possible single bit time resolution, the TDC full scale was set to 2  $\mu s$  for 10  $mm$  straws and to 5  $\mu s$  for the 20  $mm$  straws (corresponding to a single bit resolution of 0.5  $ns$  and 1.25  $ns$  respectively).

The beam intensity was appropriately lowered to have a single's count rate less than 10  $kHz$  on individual straws, consequently the probability of having multiple hits in the same trigger was negligible.

A typical drift time distribution for 10  $mm$  straws is shown in fig.10. The delay,  $T_0$ , due to signal propagation through anode, cables, preamplifier, and discriminator is determined for each channel from the starting edge of the drift time distribution. This value is subsequently subtracted from the read TDC value for all further analysis.

The field dependence of drift velocity in dimethyl ether as parametrized by [6] is

used to compute the time-to-space relationship. The  $T_0$  subtracted TDC values are accordingly transformed into drift distances for the hit straws.

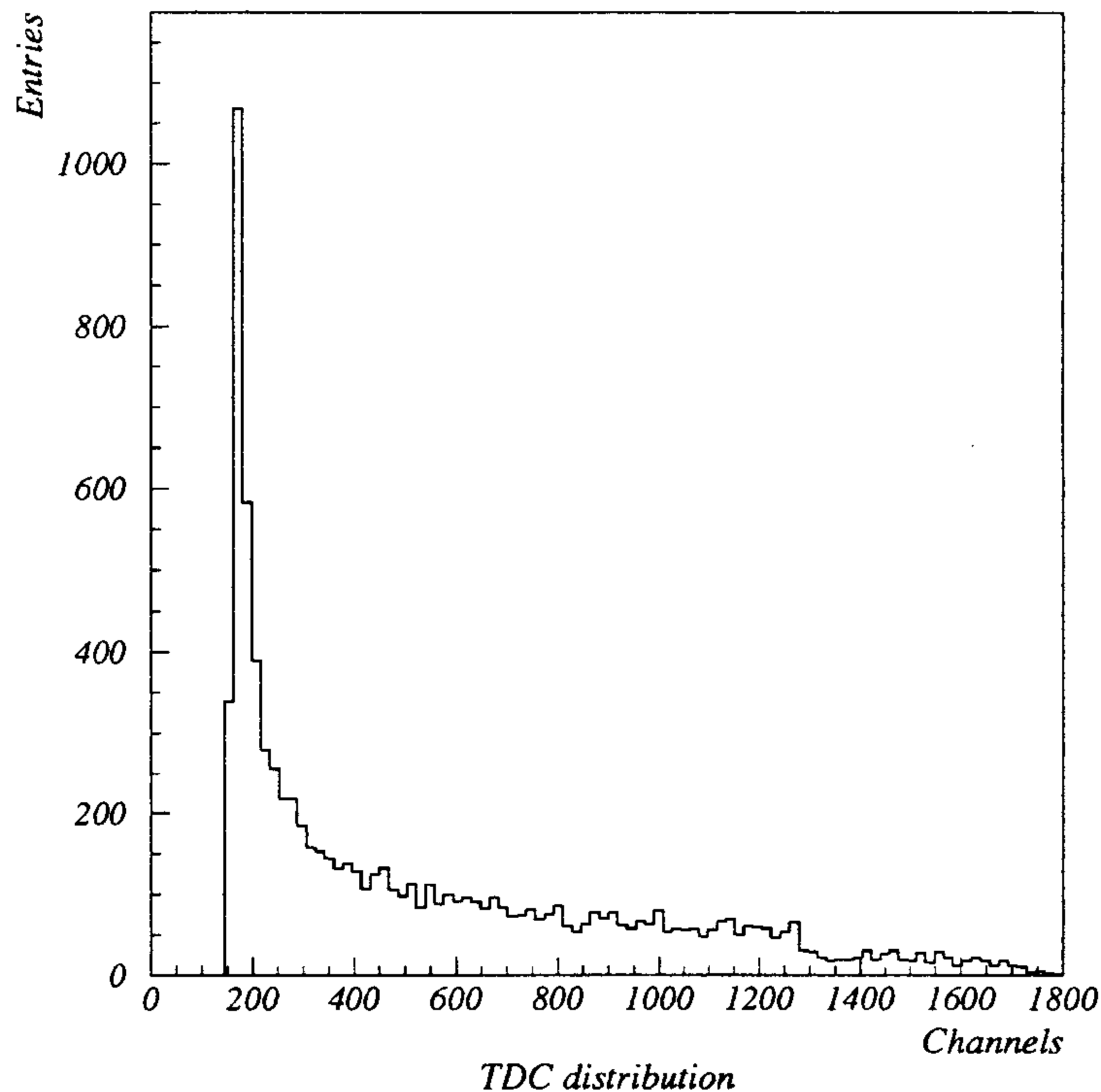


Figure 10: Typical drift time distribution for a 10 mm straw. The starting edge of the TDC distribution determines  $T_0$ .

## 5 Local space resolution

As illustrated in fig.11a, for three aligned straws the distance of closest approach for the central straw is equal to the average of the distances of closest approach for the two external straws. In order to determine the straw space resolution one can define a function  $R_a$  as:

$$R_a = (r_1 + r_2)/2 - r \quad (2)$$

where  $r$  is the drift radius measured by the central straw and  $r_1, r_2$  are the drift radii measured by the two external straws. The rms of the function  $R_a$ , denoted by  $\sigma_a$ , is related to the straw space resolution (appendix 1) by:

$$\sigma_a = \sqrt{3/2} \sigma(r) \quad (3)$$

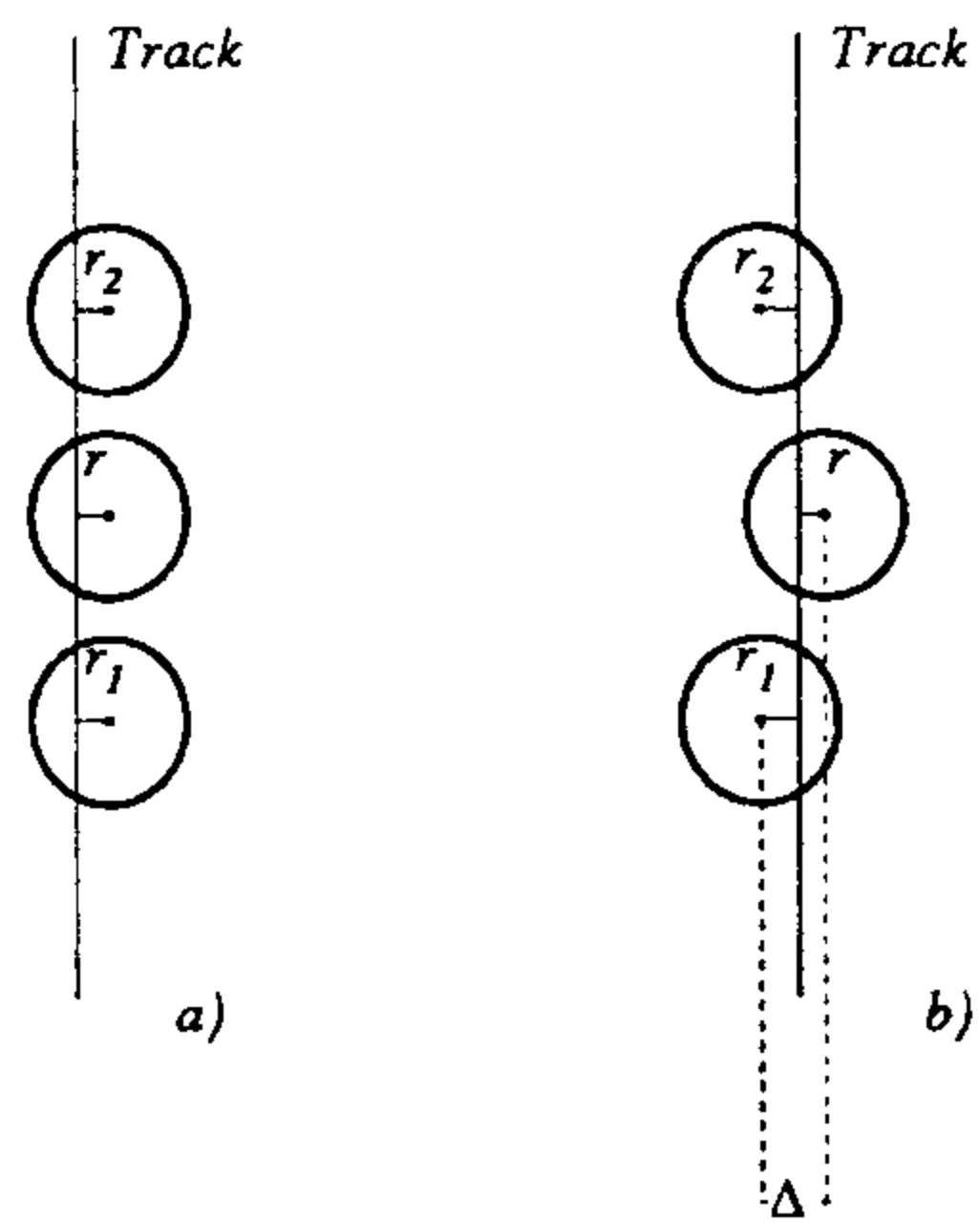


Figure 11: A graphical illustration of how to construct functions using drift radii of a) aligned and b) staggered straws to obtain straw space resolution.

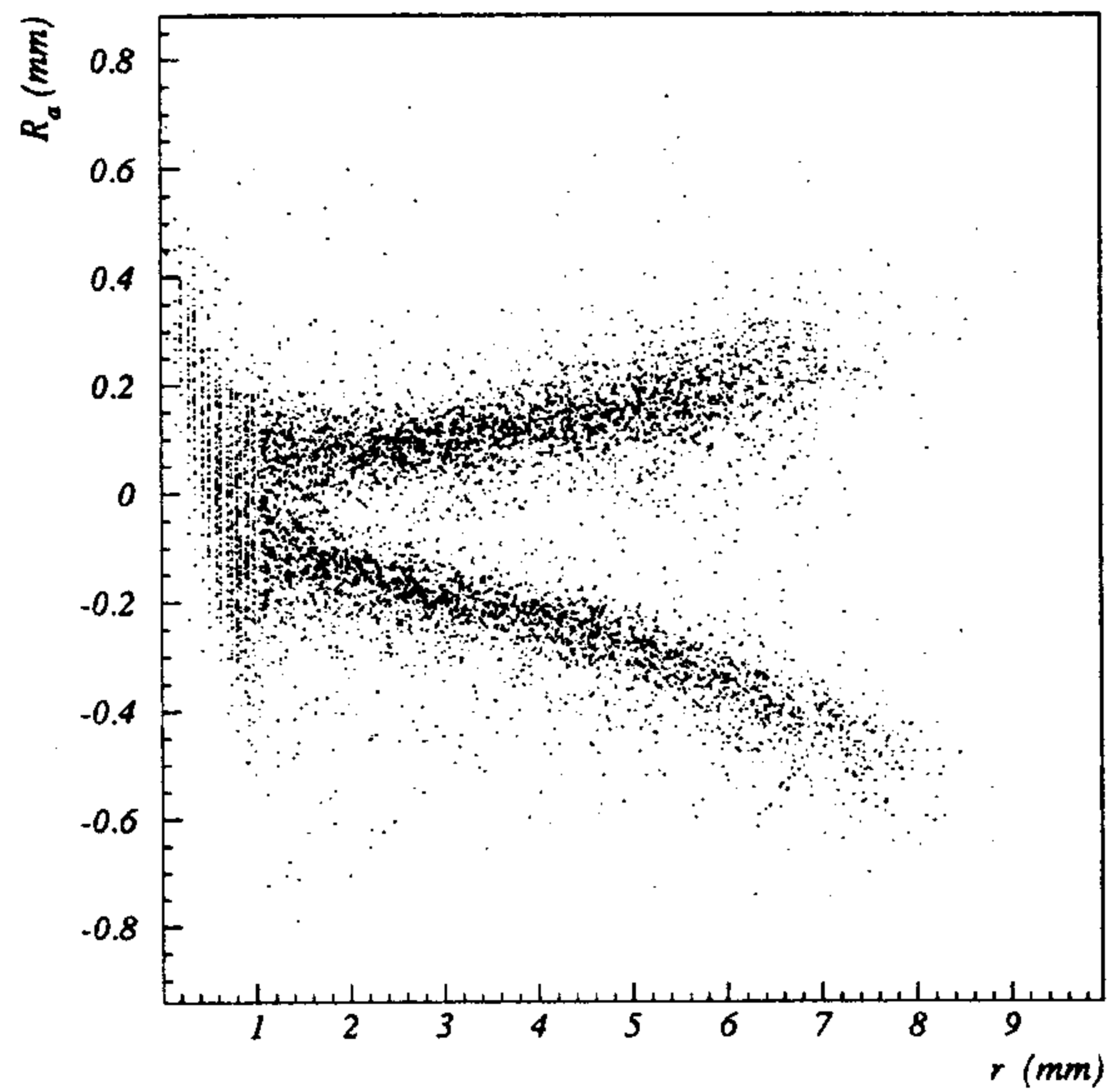


Figure 12: The scatter plot of the function  $R_a$  against  $r$  for the 20 mm straws.

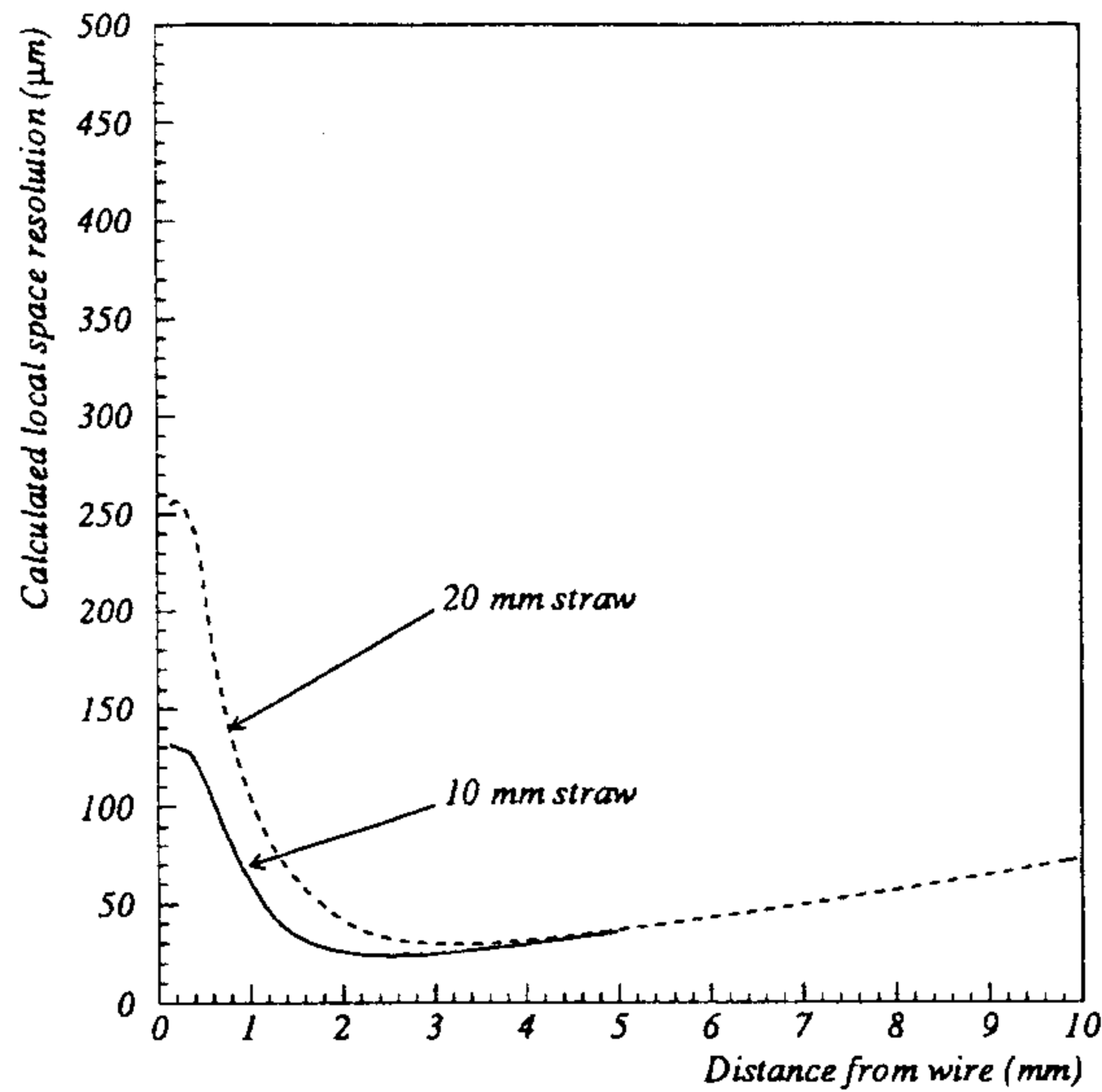


Figure 13: The calculated dependence of local space resolution on the drift distance for 10 and 20 mm straws. The curves are computed using eq.19 of appendix 2 which gives the quadratic sum of the contributions to space resolution due to electron diffusion ( $7 \mu m$  for each  $mm$  of drift), ionization statistics ( $\lambda = 160 \mu m$ ), and time jitter ( $\sigma_t$  was measured during the test beam to be  $2 ns$  and  $4 ns$  for the electronics used with the 10 mm and 20 mm straws respectively)

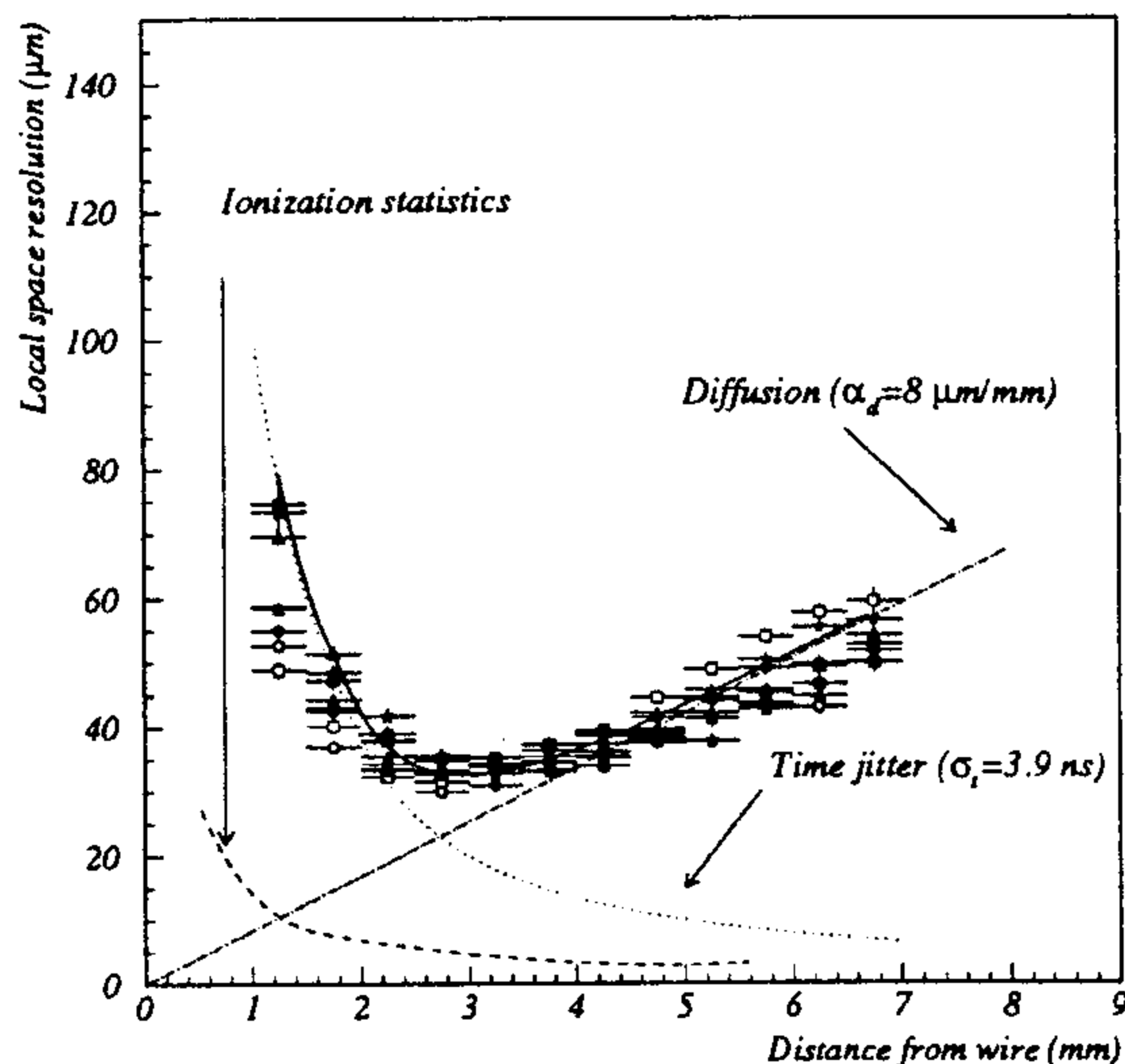


Figure 14: The dependence of local space resolution on drift distance for the 20 mm straws. The solid curve is the fit of eq.19 to the data whereas the other curves show the individual contributions to local space resolution as mentioned in appendix 2.

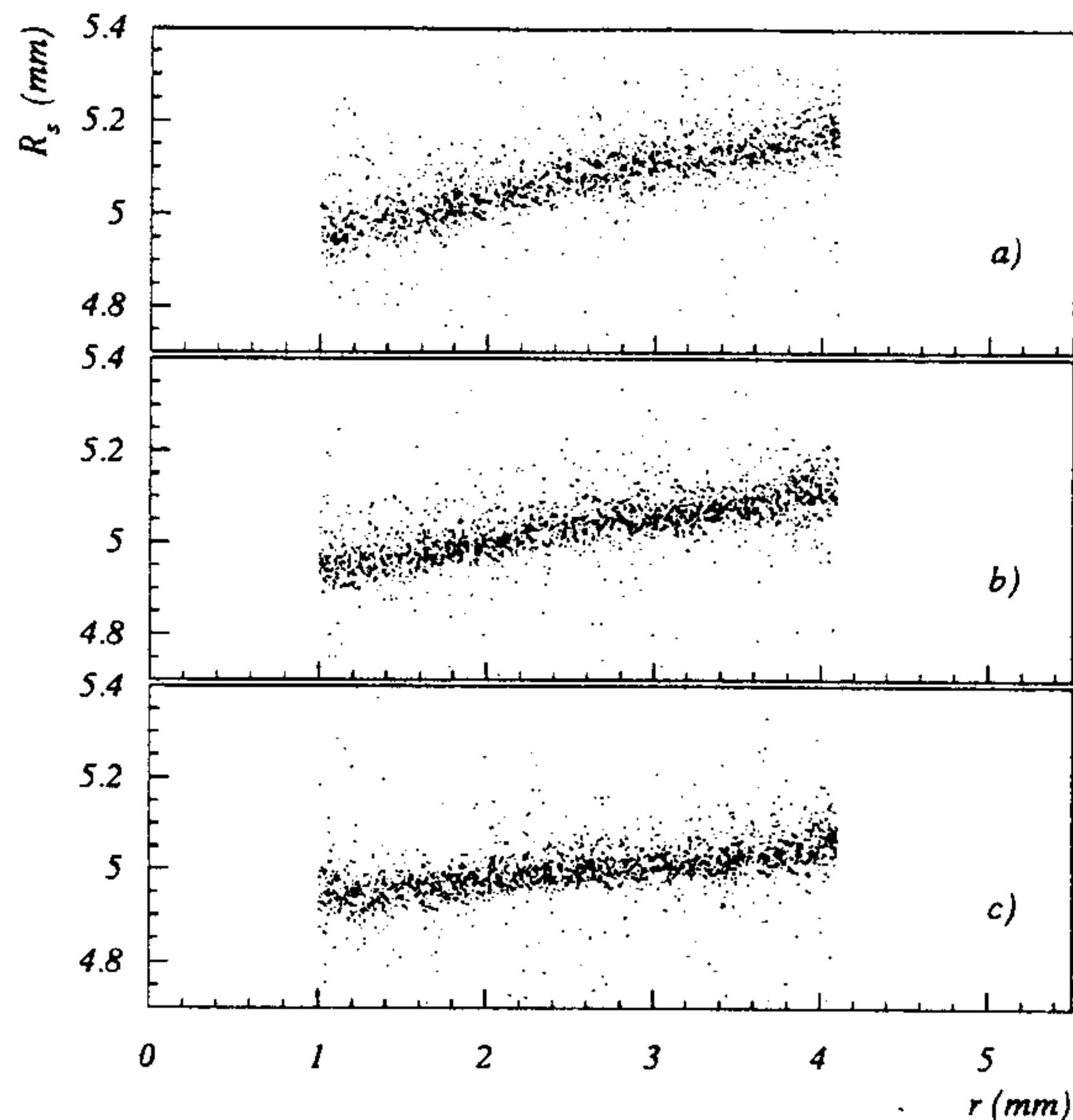


Figure 15: The scatter plots of the function  $R_s$  against  $r$  for the 10 mm straws with different values of the beam distance from the straw center. a) 8 cm, b) 50 cm, c) 80 cm

where the function  $\sigma(r)$  represents the straw space resolution at drift distance  $r$ .

In fig.12 the function  $R_a$  for three of the 20 mm straws is plotted against  $r$ . It is found that the events are divided in two principal bands. The two bands are found to be associated with tracks passing above and below the wire and this observation can be explained by a misalignment of the three wires. The fact that the average value of the function  $R_a$  for each of the two bands of fig.12 depends on  $r$  indicates the extent of systematics introduced due to wire and straw eccentricity and the corresponding lack of accuracy in the time-to-space relationship used. The systematics, if not corrected, will dominate once the straw performance over the entire radius is considered. However, considering the  $R_a$  distribution for one of the bands of fig.12 and with a fixed value of  $r$ , only the mean of the distribution is influenced by the systematics whereas the rms of the distribution is still related to *local space resolution*  $\sigma(r)$  by eq.3.

The dependence of local space resolution on drift distance is largely determined by three factors: diffusion of electrons, the variation in the distance between adjacent clusters given by ionization statistics, and jitter in time measurements introduced by used electronics. The detailed considerations of the three contributions are given in appendix 2 and the computed dependence of the local space resolution on drift distance for 10 and 20 mm straws is shown in fig.13. For the major part of the straw radius the local space resolution is expected to be smaller than 50  $\mu\text{m}$ , and there is a sharp deterioration in local space resolution as one approaches the wire (smaller drift distances). For drift distance greater than 2~3 mm, the local space resolution

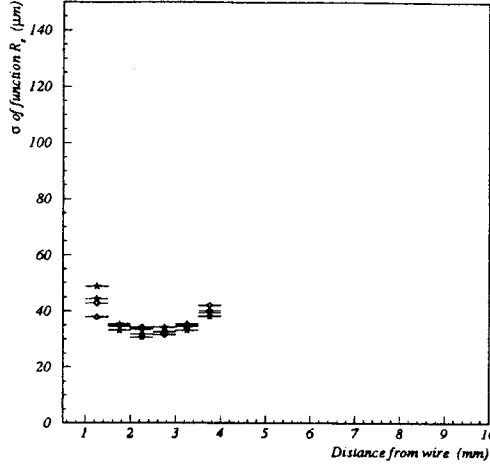


Figure 16: The rms of the function  $R_s$  for the 10 mm straws.

degrades almost linearly with increasing drift radius.

To determine the local space resolution from data, the two bands of fig.12 are divided in small bins of  $r$  and the corresponding distributions for function  $R_a$  are obtained. As the separation of the two bands is only possible for drift distances greater than 1 mm, smaller drift distances are ignored in all the subsequent results. As implied by eq.3, the local space resolution  $\sigma(r)$  for the 20 mm straws is obtained from the  $\sigma_a$  values, as determined by Gaussian fits to the  $R_a$  distributions and is shown in fig.14. The results shown in fig.14 correspond to different straws and different distances of the beam along the wire axis and they all show the same dependence of local space resolution on drift distance. The contributions to the local space resolution due to diffusion, ionization statistics, and time jitter are separated from each other by fitting the data shown in fig.14 with eq.19. The dependence of local space resolution on drift distance is found to be in agreement with the phenomenological model as discussed in appendix 2. As shown in fig.14, for drift distances smaller than  $\sim 3$  mm the dominant contribution to the local space resolution comes from jitter of time measurements, whereas for longer drift distances, local space resolution is largely determined by electron diffusion.

For the 10 mm staggered straw, a function  $R_s$  (fig.11b) can be defined where:

$$R_s = (r_1 + r_2)/2 + r \quad (4)$$

As given in appendix 1, the rms of the function  $R_s$ , denoted by  $\sigma_s$ , is related to local space resolution  $\sigma(r)$  by:

$$\sigma_s = \sqrt{\frac{\sigma^2(\Delta - r)}{2} + \sigma^2(r)} \quad (5)$$

where  $\Delta$  (nominally 5.1 mm for the prototype) is the stagger distance between the straws. The function  $R_s$  is expected to have an average value equal to  $\Delta$ . The scatter

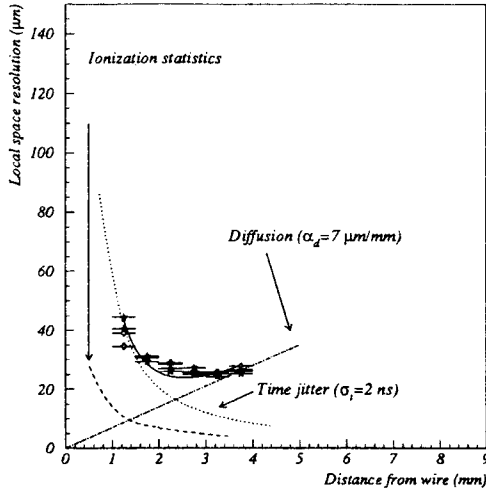


Figure 17: The dependence of local space resolution on drift distance for the 10 mm straws. The solid curve is the fit of eq.19 to the data whereas the other curves show the individual contributions to local space resolution as mentioned in appendix 2.

plots of the function  $R_s$  and the drift radius of the central straw are shown in fig.15 for different values of the beam position along the straw axis. The dependence of the average value of the function  $R_s$  on drift radius is strongest at the center of the straw and decreases as one moves towards the straw end. This is explained by the fact that the straw eccentricity also has a similar dependence on distance along the straw axis.

To determine the local space resolution for 10 mm straws the scatter plots shown in fig.15 are divided in small bins of  $r$  and the distributions for the  $R_s$  are obtained. The  $\sigma_s$  values, as obtained by Gaussian fits to these distributions, are plotted in fig.16 against  $r$ . The local space resolution  $\sigma(r)$  is obtained from the  $\sigma_s$  values by inverting eq.5 (appendix 1) and is shown in fig.17. The contributions to the local space resolution due to diffusion, ionization statistics, and time jitter are separated from each other by fitting the data shown in fig.17 with eq.19 and the fit results are shown in the same figure.

## 6 Correction for systematics

The method used in the previous section to determine the local space resolution considers tracks passing within a small interval of drift radius and is therefore relatively immune from systematics. Typically, as in the scatter plot of fig.15b, the local spread of points ( $\sigma \sim 40 \mu m$ ) is much less than the variation of average value of the function  $R_s$  ( $\sim 150 \mu m$ ) over the range of drift radius from 1 mm to 4.1 mm. The corresponding distribution of the function  $R_s$  for all the tracks (the drift radius for the given range,  $1 \text{ mm} \leq r \leq 4.1 \text{ mm}$ , has a uniform distribution) is shown in fig.18a

and is found to have an rms of  $65 \mu m$  as determined by a Gaussian fit. Fig.18b shows the expected distribution of the function  $R_s$ , as simulated for a straw which is free of systematics. The result shown in fig.18b is obtained for tracks with drift radius uniformly distributed from  $1 mm$  to  $4.1 mm$  and using the dependence of local space resolution on drift radius of fig.17. The rms of the distribution, as determined by a Gaussian fit, is a factor two less than that of the distribution of fig.18a. This is quite as expected because the rms of the  $R_s$  distribution of fig.18a is determined by both the stochastic and systematic contributions to the straw performance.

The *global space resolution* is defined as  $\sqrt{2/3}$  times the rms of the  $R_s$  distribution for tracks passing from  $1 mm$  to  $4.1 mm$ . Its values, as determined by a Gaussian fit, for different beam positions along the straw axis are given in fig.19. The global resolution is  $\sim 30 \mu m$  when the beam is close to the straw end, and degrades up to  $60 \mu m$  when the beam is at the center of the straws.

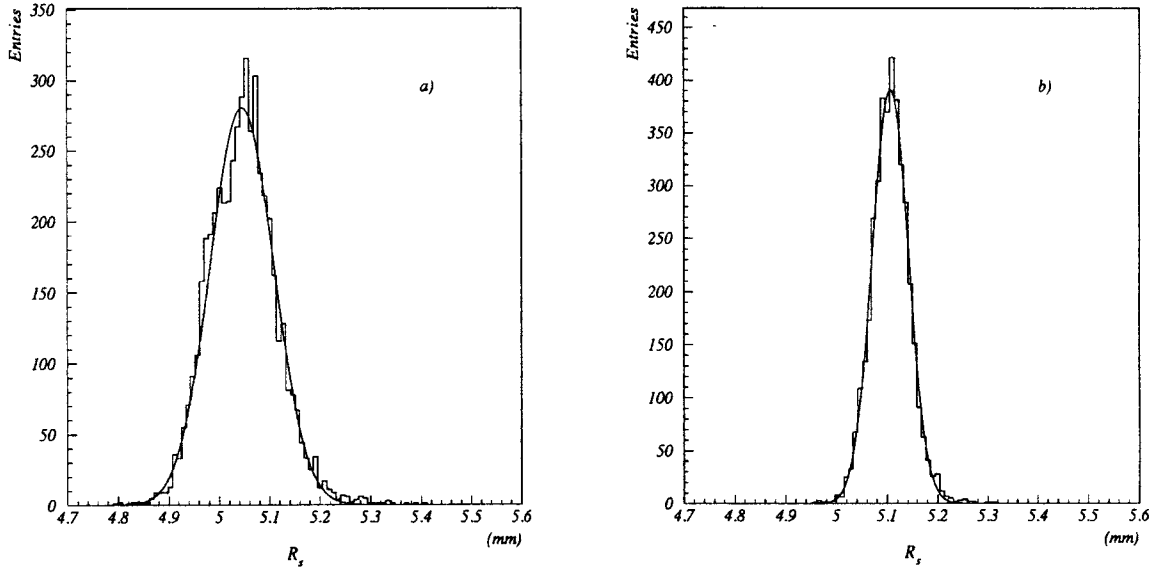


Figure 18: a) The distribution of the function  $R_s$  for all the events of fig.15b. b) The expected distribution of the function  $R_s$ , as obtained from simulation for straws free of systematics.

For the prototype straws a maximum eccentricity up to  $300 \sim 600 \mu m$  is expected (appendix 3). A simple method can be used to experimentally determine the straw eccentricity and correct for the corresponding systematic effects. For the test beam data the tracks passing above and below the wire can be separated and the corresponding TDC distributions are shown in fig.20. The straw eccentricity creates an asymmetry in the electric field resulting in zones of low and high field as compared with an ideally concentric straw. The behaviour of the TDC distributions of fig.20 is qualitatively evident. The drift velocity is lower than the ideal case for the tracks passing through the low field region (below the wire) and therefore the TDC distri-



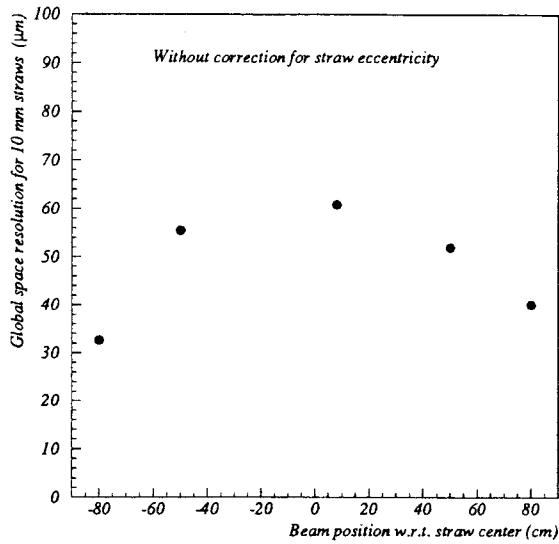


Figure 19: The global space resolution for the 10 mm straws for different beam positions along the straw axis.

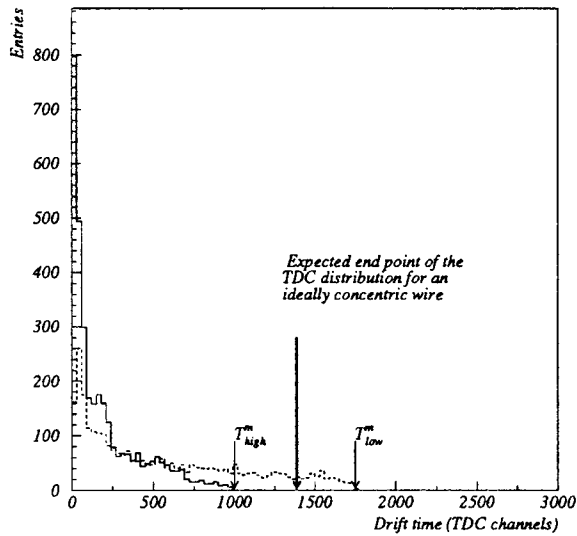


Figure 20: The TDC distributions for tracks passing above (solid histogram) and below the wire (dashed histogram).

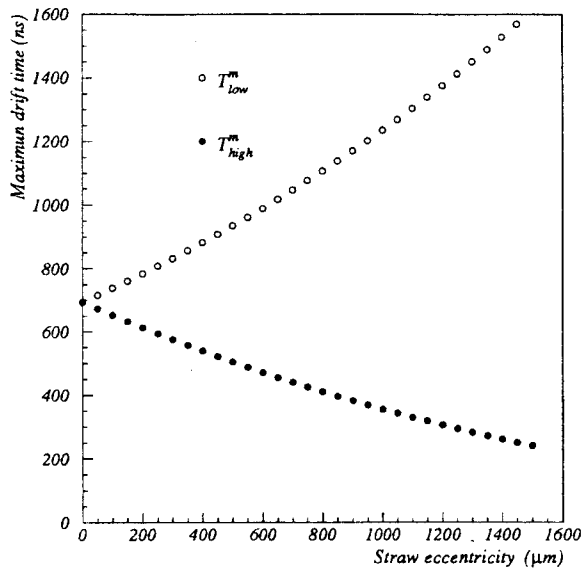


Figure 21: The calculated end point of the TDC distributions for the high and low field zones as a function of straw eccentricity.

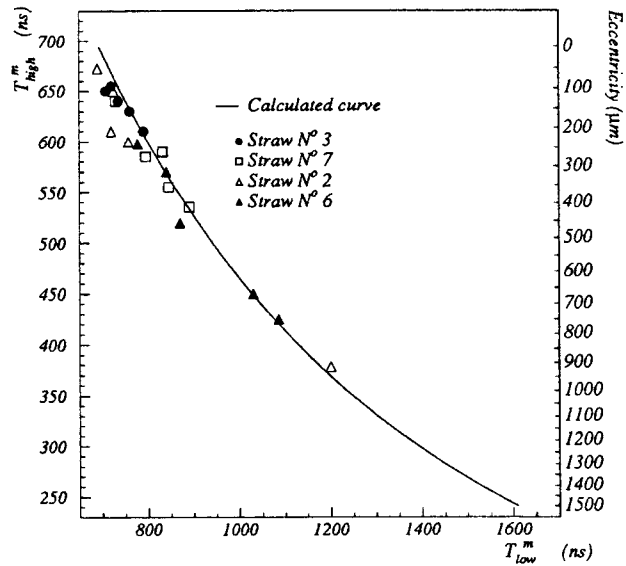


Figure 22: Determination of straw eccentricity from the end points of TDC distributions for the high and low field zones.

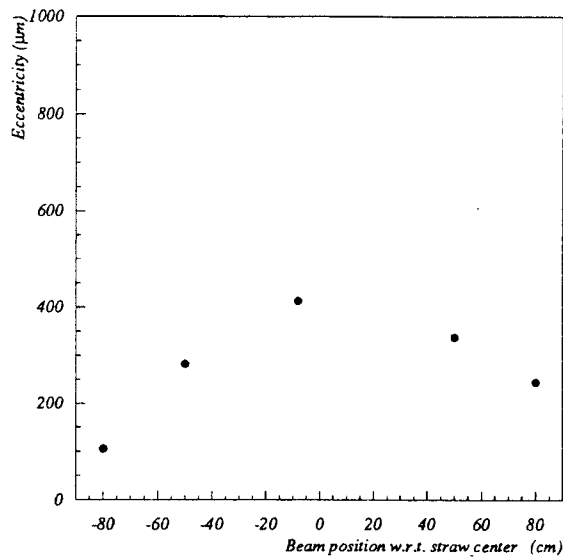


Figure 23: A typical straw eccentricity as a function of distance from the straw center. The eccentricity is determined from the end points of the TDC distributions.

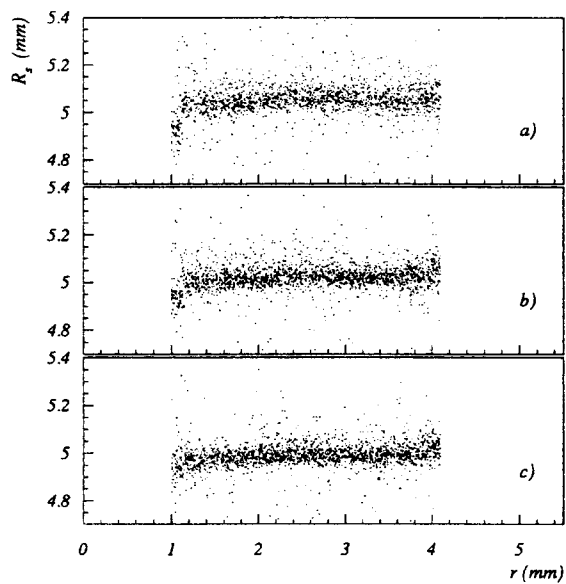


Figure 24: The scatter plots of the function  $R_s$  against  $r$  for the 10 mm straws after having corrected for straw eccentricity. The beam distance from the straw center is a) 8 cm, b) 50 cm, c) 80 cm.

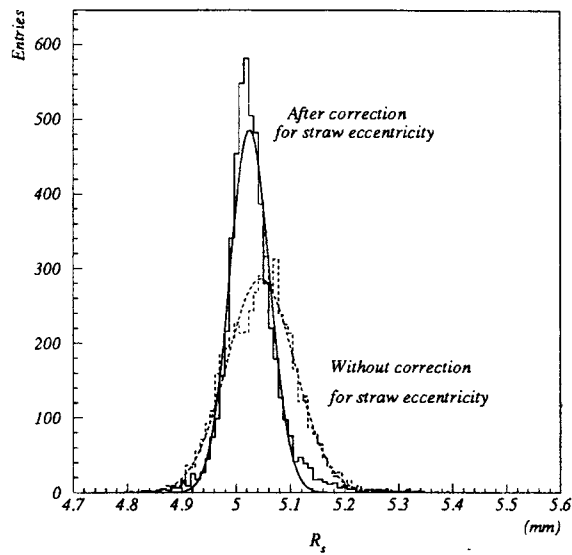


Figure 25: The distribution of the function  $R_s$  for the 10 mm straws with (solid histogram) and without (dashed histogram) correcting for systematics. The solid histogram has a  $\sigma$  of  $36 \mu\text{m}$  and its average value is  $5.02 \text{ mm}$  ( $0.08 \text{ mm}$  less than the nominal value of  $\Delta$  due to mechanical imprecision).

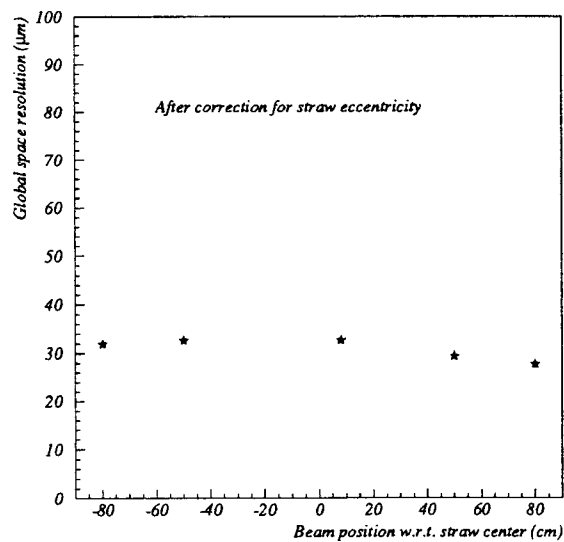


Figure 26: Global space resolution for the 10 mm straws after having corrected for systematics for different beam positions along the straw axis.

bution extends beyond the maximum value for the ideal case. On the other hand, the drift velocity is higher than the ideal case for the tracks passing through the high field region (above the wire) and correspondingly the TDC distribution terminates before the maximum value for the ideal case. The electric field for an eccentric straw can be computed by using the method of images and the calculated end points of the TDC distribution for the high and low field regions ( $T_{high}^m$  and  $T_{low}^m$  respectively) as a function of the straw eccentricity are shown in fig.21. In fig.22 the correlation between  $T_{high}^m$  and  $T_{low}^m$  values for different values of straw eccentricity are shown together with experimental data for different straws and for different values of the beam distance from the straw center. By observing the  $T_{high}^m$  and  $T_{low}^m$  values, the eccentricity for each straw can therefore be determined (fig.23).

Once the eccentricity is known, the electric field and the corresponding time-to-space relationship can be computed correctly. The influence of such a correction algorithm is shown in fig.24 where the scatter plot of the function  $R_s$  is plotted against drift distance  $r$ . A comparison of fig.24 with fig.15 shows that the systematic dependance of the mean of the  $R_s$  distribution on drift radius  $r$  is eliminated when one uses the time-to-space resolution computed for the eccentric straw. An improvement of a factor two in the global space resolution is obtained (fig.25). The global space resolution, obtained from the function  $R_s$  distribution, after having corrected for the straw eccentricity for different values of the beam position along the straw axis is shown in fig.26. Fig.26 shows that a global space resolution of  $30 \mu m$  can be reached and is well maintained for the entire straw length.

The results presented in fig.26 are relevant to drift radius ranging from  $1 mm$  to  $4.1 mm$ . This restriction on drift radius can be removed and the distribution of the function  $R_s$  over the entire straw radius and over different beam positions along the straw axis, is shown in fig.27. The rms of this distribution, which now contains also the tracks passing very close to the wire ( $r < 1 mm$ ) where the local resolution is relatively poor, still shows a space resolution of  $39 \mu m$ .

## 7 Conclusions

The first FINUDA straw tube prototype has been constructed and successfully tested for its performance evaluation. While operating with pure dimethyl ether, gas gain of  $10^7$ - $10^8$  can be reached with typical signals having a fast rise time of a few nano seconds. The single's count rate plateau is longer than 800 V.

The dependence of local space resolution on drift distance is found to be in agreement with a simple model considering contributions due to electron diffusion, ionization statistics and jitter in time measurements. The contribution due to electron diffusion is about  $7 \mu m$  for each mm of drift distance. At drift distances smaller than  $2\sim 3 mm$ , the contribution due to jitter in time measurements dominates the space resolution.

The straw length is an important parameter in determining the eccentricity and consequently the systematics and the space resolution. The straw eccentricity can

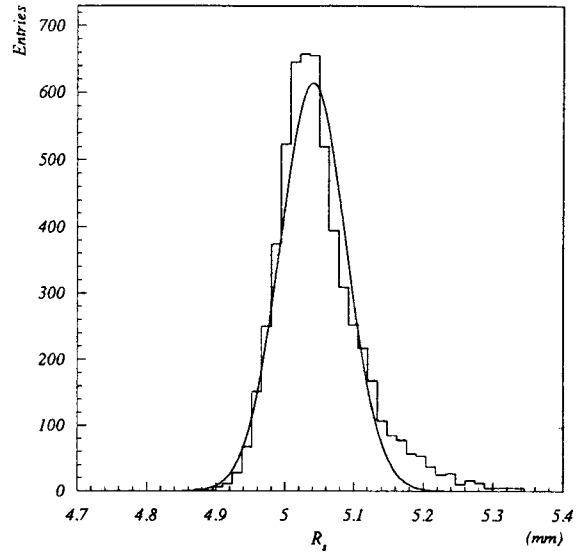


Figure 27: The distribution of the function  $R_s$ , over the entire straw radius and over different beam positions along the straw axis, for the 10 *mm* straws.

be measured from the drift time distributions and the systematics introduced by eccentricity can be corrected. With such a correction procedure, for the first time with 2 *m* long straws, a space resolution better than 40  $\mu\text{m}$  has been obtained.

## 8 Acknowledgements

We are thankful to the SPECAS group of the LNF, for their technical help in making of the mechanical components of the prototype. We also appreciate the helpful support of G. Corradi in designing the preamplifier boards. Special thanks are due to S. Marcello, B. Minetti, M.R. Mondardini, and R.De Salvo for their help during the data taking at the test beam.

## Appendix 1: Space resolution and the rms of functions $R_a$ and $R_s$

The function  $R_a$  for the aligned straws is defined as:

$$R_a = (r_1 + r_2)/2 - r \quad (6)$$

The assumption that the three straws have the same dependence of the space resolution on the drift distance given by function  $\sigma(r)$ , combined with a simple application of the error propagation formula [7] based on Taylor series expansion of functions, gives:

$$\sigma_a = \sqrt{\frac{\sigma^2(r_1)}{4} + \frac{\sigma^2(r_2)}{4} + \sigma^2(r)} \quad (7)$$

where  $\sigma_a$  represents the rms of the function  $R_a$ . As the test beam tracks were almost parallel to the y-axis,  $r \sim r_1 \sim r_2$  and therefore  $\sigma(r) \sim \sigma(r_1) \sim \sigma(r_2)$ , yields:

$$\sigma_a = \sqrt{3/2}\sigma(r) \quad (8)$$

The  $\sigma_a$  is obtained from the experimental data and the  $\sigma(r)$  can then be determined.

The function  $R_s$  for the staggered straws is defined as:

$$R_s = (r_1 + r_2)/2 + r \quad (9)$$

and the rms of the function  $R_s$  is given by:

$$\sigma_s = \sqrt{\frac{\sigma^2(r_1)}{4} + \frac{\sigma^2(r_2)}{4} + \sigma^2(r)} \quad (10)$$

For the staggered straws seen by tracks almost parallel to y-axis,

$$r_1 \sim r_2 \sim \Delta - r \quad (11)$$

where  $\Delta$  is the stagger distance between the straws. A substitution of relation 11 in eq.10 gives:

$$\sigma_s = \sqrt{\frac{\sigma^2(\Delta - r)}{2} + \sigma^2(r)} \quad (12)$$

The dependence of  $\sigma_s$  on drift radius is shown in fig.16. To invert eq.12 a function  $f(r)$  (a third order polynomial in  $r$ ) is used to approximate  $\sigma(r)$  and the data of fig.16 is first fitted by a function  $S(r)$ , where:

$$S(r) = \sqrt{\frac{f^2(\Delta - r)}{2} + f^2(r)} \quad (13)$$

The deconvoluted local space resolution as shown in fig.17 is then obtained by:

$$\sigma(r) = \frac{f(r)}{S(r)}\sigma_a \quad (14)$$

## Appendix 2: Contributions to local space resolution

The drifting electrons in pure dimethyl ether are expected to remain at thermal energies, and the spread along drift direction has a  $\sigma$  given by:

$$\sigma_d^2(r) = \int_0^r \frac{2kT}{eE} dr_1 \quad (15)$$

where  $k$  is the Boltzmann constant,  $T$  is the gas temperature,  $e$  is the electronic charge and  $E$  is the electric field. Substituting for radius dependence of electric field in the straw and integrating the above equation we get:

$$\sigma_d(r) = \sqrt{\frac{kT \ln(r_s/r_w)}{eV}} r = \alpha_d r \quad (16)$$

The expected value of  $\alpha_d$  is  $\sim 7 \times 10^{-3}$  for our operating conditions; i.e about  $7 \mu m$  of electron diffusion for each  $mm$  of drift distance. The assumption that drifting electrons remain at thermal energies is violated at very small drift distance where the electric field has very high values. Therefore the value of  $\sigma_d$  as given above should be interpreted as a lower limit on contribution due to electron diffusion.

The distance between successive clusters has an exponential distribution with an average value  $\lambda$ , calculated to be  $160 \mu m$  for dimethyl ether at standard conditions. The distance of closest approach for the track passing at drift distance  $r$  from the wire is on the average overestimated by  $\sqrt{r^2 + (\lambda/2)^2} - r$ . The contribution to space resolution due to ionization statistics, is given by rms of the variable  $\sqrt{r^2 + (d/2)^2} - r$ :

$$\sigma_i(r) = \sigma_{(\sqrt{r^2 + (d/2)^2} - r)} \quad (17)$$

where  $d$  is the distance between successive clusters. The  $\sigma_i$  as a function of drift radius is numerically evaluated and parametrized. For the above mentioned value of  $\lambda$ ,  $\sigma_i$  is found to be less than  $80 \mu m$  for tracks passing very close to the wire and is less than  $10 \mu m$  for tracks passing at a distance greater than  $1 mm$  from the wire.

A constant jitter in time measurements,  $\alpha_t$  contributes to straw space resolution as:

$$\sigma_t(r) = v_d(r) \alpha_t \quad (18)$$

where  $v_d$  is the drift velocity at  $r$ .

The dependence of space resolution for 20 and 10  $mm$  straws as shown in fig.14 and fig.17 are fitted with the function:

$$\Sigma(r) = \sqrt{\sigma_d^2(r) + \sigma_i^2(r) + \sigma_t^2(r)} \quad (19)$$

with  $\alpha_d$ , and  $\alpha_t$  as free parameters. The value of parameter  $\lambda$  giving the contribution due to ionization statistics is fixed to  $160 \mu m$ . For drift distances smaller than  $2 \sim 3$



$mm$  the dominant contribution to space resolution comes from jitter in time measurements, whereas for longer drift distances, space resolution is largely determined by electron diffusion. In principle the fit can even be performed leaving  $\lambda$  as a free parameter, but as in our data the contribution due to ionization statistics never dominates the space resolution, the fit is not much sensitive to the value of  $\lambda$ . On the other hand at our operating conditions the gas gain is sufficiently high to overrule the possibility that we have a single cluster efficiency much less than unity and therefore  $\lambda$  should be expected to be very close to the nominal value. In fact a fit performed with  $\alpha_d$ ,  $\alpha_t$  and  $\lambda$  as free parameters gives  $\lambda$  to be statistically compatible with  $160 \mu m$ .

### Appendix 3: Straw eccentricity due to gravity and electrostatics

Considering only the gravitational forces on a wire of length  $2L$ , with the two ends on the same horizontal position and pulled to a tension  $T$ , the wire catenary,  $y(x)$ , is given by:

$$y(x) = \frac{T}{\rho} \left( \cosh \frac{\rho x}{T} - 1 \right) \quad (20)$$

where  $\rho$  is the linear weight density of the wire and  $x$  is the coordinate along the wire axis. For very small sag to span ratio, as in our case, the catenary can be well approximated by a parabola:

$$y(x) = \frac{\rho x^2}{2T} \quad (21)$$

and the gravitational sag  $S_g$  is given by:

$$S_g = \frac{\rho L^2}{2T} \quad (22)$$

For  $30 \mu m$  tungsten wire, pulled by a tension of  $1 N$ , the expected gravitational sag is  $\sim 70 \mu m$ .

The same relation (eq.22) can be applied to straw catenary where  $\rho$  now becomes the linear weight density of the straw and the gas. The gas weight contributes significantly to linear weight density of the straw ( $\sim 12\%$  for  $10 mm$  straws and  $\sim 25\%$  for  $20 mm$  straws). For a two meter straw, tensioned to  $25 N$ , the expected gravitational sag is  $300 \mu m$  for the  $10 mm$  diameter straw and it is  $660 \mu m$  for a  $20 mm$  diameter straw.

As centers of the wire and straw follow two different curves, electrostatic forces deform the wire position from a simple parabolic curve. The electrostatic forces, in the  $y$  direction, per unit wire length are given by:

$$F_e = k\delta \quad (23)$$

where  $\delta$  is the distance between straw and wire centers. With anode wire kept at  $V$  volts the constant  $k$  is given by:

$$k = \frac{V^2}{2} \frac{dC}{d\delta} = 2V^2 \pi \epsilon_0 (r_s \ln(r_s/r_w))^{-2} \quad (24)$$

where  $r_s$  and  $r_w$  are straw and wire radii. The mechanical restoring force per unit wire length due to wire tension  $T_w$  is given by:

$$F_t = T_w \frac{d^2 y_w(x)}{dx^2} \quad (25)$$

where  $y_w(x)$  represents the static wire position. The differential equation governing the static wire position is:

$$T_w \frac{d^2 y_w(x)}{dx^2} + k [y_w(x) - y_s(x)] - \rho_w = 0 \quad (26)$$

where  $\rho_w$  is the linear weight density of the wire and  $y_s(x)$  is the catenary of the straw. Assuming that the straw position is unaffected by electrostatic forces the straw catenary can be approximated by a parabola:

$$y_s(x) = \frac{\rho_s x^2}{2T_s} \quad (27)$$

Substituting eq.27 in eq.26 and solving for  $y_w(x)$  for a straw supported at the two ends with concentric pins one gets:

$$y_w(x) = \frac{\rho_s x^2}{2T_s} - \eta \left( \frac{\cos \sqrt{k/T_w} x}{\cos \sqrt{k/T_w} L} - 1 \right) \quad (28)$$

where:

$$\eta = \frac{T_s \rho_w - T_w \rho_s}{k T_s} \quad (29)$$

The reference frame, while solving eq.26, is taken to have its origin at the center of the straw with  $x$  representing the coordinate along the straw axis.

The straw eccentricity, given by the difference of straw center (eq.27) and the center of the wire (eq.28) can now be computed. Using the straw and wire mechanical tensions as given in section 2 with anode voltages as mentioned in section 4, the maximum straw eccentricity, at the straw center, is 320  $\mu m$  for the 10 *mm* straws and 630  $\mu m$  for the 20 *mm* straws.

## References

- [1] The FINUDA Collaboration. (M. Agnello et. al.) **FINUDA A detector for nuclear physics at DAΦNE**, LNF report. LNF-93/021 (IR). 1993
- [2] M. Agnello et. al., **FINUDA Technical Proposal**, 1994. To be published.
- [3] Straws were produced by Lamina Dielectrics Ltd. Myrtle Lane, Billingshurst West Sussex England.
- [4] Wire produced by Luma Metall AB. Box 701. S-391 27 Kalmar Sweden.
- [5] The conductive glue used for the prototype is product 3M-106 produced by 3M Italia S.p.A. 20090 Segrate San Felice (MI) Italy.
- [6] G. Bari et. al., *Nucl. Instr. and Meth.* **A251**, (1986) 292
- [7] Review of Particle Properties, *Phys. Rev.* **D50**, (1994) 1282